






RESEARCH ARTICLE | NOVEMBER 17 2023

Computational study of lateral jet interaction in hypersonic thermochemical non-equilibrium flows using nonlinear coupled constitutive relations

Shuhua Zeng (曾舒华) ; Junyuan Yang (杨俊沅); Wenwen Zhao (赵文文)  ; Yifeng Huang (黄依峰); Zhongzheng Jiang (江中正) ; Weifang Chen (陈伟芳) 

 Check for updates

Physics of Fluids 35, 116117 (2023)

<https://doi.org/10.1063/5.0177540>


View
Online


Export
Citation

08 April 2024 03:59:57



APL Energy

Latest Articles Online!

Read Now

 AIP
Publishing

 AIP
Publishing

Computational study of lateral jet interaction in hypersonic thermochemical non-equilibrium flows using nonlinear coupled constitutive relations

Cite as: Phys. Fluids **35**, 116117 (2023); doi: 10.1063/5.0177540

Submitted: 22 September 2023 · Accepted: 27 October 2023 ·

Published Online: 17 November 2023



View Online



Export Citation



CrossMark

Shuhua Zeng (曾舒华),¹ Junyuan Yang (杨俊沅),¹ Wenwen Zhao (赵文文),^{1,2,a)} Yifeng Huang (黄依峰),³ Zhongzheng Jiang (江中正),^{1,2} and Weifang Chen (陈伟芳)^{1,2}

AFFILIATIONS

¹School of Aeronautics and Astronautics, Zhejiang University, Hangzhou 310027, China

²Huanjiang Laboratory, Zhuji 311800, China

³State Key Laboratory of High Temperature Gas Dynamics, Institute of Mechanics, Chinese Academy of Sciences, Beijing 100190, China

^{a)}Authors to whom correspondence should be addressed: wvzhao@zju.edu.cn

ABSTRACT

The present study reports the numerical analyses of lateral jet interaction around a Terminal High Altitude Area Defense-type (THAAD-type) model in hypersonic rarefied flows, with the real gas effect incorporated. The computation approach employed is the recently developed thermochemical non-equilibrium nonlinear coupled constitutive relations (NCCR) model. Regarding the simulation conditions, the flight velocity and height are set to 20 Ma and 80 km, respectively. To disclose the flow mechanism of lateral jet interaction, the complex flowfield characteristics and surface pressure distributions are discussed at length. Additionally, the research explores the impact of two key factors, namely, the jet pressure ratio and the jet Mach number, on the control performance of an in-flight vehicle's reaction control system (RCS). The results demonstrate that the complicated flowfield structures in lateral jet interaction are successfully reproduced by the NCCR model. With an increase in either the jet pressure ratio or the jet Mach number, the force and moment amplification factors decrease, while the absolute value of the normal force coefficient increases. Notably, it is found that the rarefied gas effect captured by the NCCR model against the Navier–Stokes–Fourier solution affects the lateral jet interaction flowfield, e.g., weakening the compressibility of the barrel shock and the expansibility of the Prandtl–Meyer expansion fan, as well as strengthening the jet wraparound effect. Importantly, the rarefied gas effect also exerts a prominent influence on the performance of RCS, with the degree of influence diminishing as the jet Mach number or the jet pressure ratio increases.

Published under an exclusive license by AIP Publishing. <https://doi.org/10.1063/5.0177540>

I. INTRODUCTION

The complex flow phenomena induced by lateral jet flow to interactions with crossflows are prevalent in aerospace applications, such as scramjet engine structures,¹ plasma stealth technology,² and attitude and orbit control of supersonic interceptor missiles.³ The reaction control system (RCS) of near-space hypersonic vehicles, which employs lateral jet technology, has garnered considerable interest from international research communities over recent decades.^{4–6} The RCS, which utilizes one or more lateral jets, generates the necessary aerodynamic force for vehicle maneuverability and flight stability, outstripping conventional aerodynamic control surfaces in control efficiency and response time in high-speed, low-density airflows at high altitudes.⁷ An additional advantage of RCS is the absence of drag and flowfield

disturbances when inactive.⁸ However, when active, the intense interaction of the lateral jet flow with high-speed crossflow results in complex flow phenomena⁹ and a reaction control force with components derived from the jet thrust and changes in surface pressure distribution on the vehicle due to lateral gas flow ejection.¹⁰ Thus, the lateral jet interaction significantly influences vehicle aerodynamics and aeroheating and could cause control reversal, generating a net force opposing the jet thrust.¹¹ Comprehensive research into lateral jet interaction with high-speed crossflow is therefore essential for optimizing the benefits of RCS in the design of hypersonic near-space vehicles.

The first elucidation of lateral jet interaction in a crossflow by Morkovin *et al.*¹² was followed by substantial work on the subject, summarized in reviews by Karagozian¹³ and Mahesh.⁹ Recent research

has focused on the physical mechanisms underlying the lateral jet flowfield¹⁴ and engineering applications of lateral jets in high-speed crossflows for the RCS of near-space hypersonic vehicles.⁵ Therein, a variety of wind tunnel experimental methods have been utilized to study the lateral jet flow in high-speed crossflow, e.g., particle image velocimetry (PIV),¹⁵ laser Doppler velocimetry,¹⁶ and Schlieren photography,¹² nevertheless, detailed flow measurements and flow visualizations are very difficult and challenging owing to the complexity of this type of lateral jet flow. Along with the development of computational fluid dynamics (CFD) and computer hardware, more and more scholars have done extensive research on the lateral jet flow or RCS through numerical modeling approaches, where Navier–Stokes–Fourier (NSF) equations with or without the turbulence models are mainly employed in the low-altitude continuum regions¹⁷ as well as direct simulation Monte Carlo (DSMC) is the dominating method for extremely rarefied flows.⁵ The flow regimes are typically determined by the Knudsen number, which is defined as the ratio of gas molecule mean free path to the characteristic length of the studied problems, and they are divided into four different flow regimes, viz., continuum regime, slip regime, transition regime, and free molecular flow regime. When the flight height of near-space vehicles increases, the density of high-speed freestreams sharply drops and the rarefied gas effect should not be ignored.⁴ Furthermore, while the freestream is in the slip or transition regimes, the core area of lateral jet flows may still be in the range of continuum regions. Regarding this type of multi-scale lateral jet flow, where the local thermodynamically equilibrium assumption fails, the NSF equations that are based on the continuum hypothesis may lose their validity to describe accurately the complex and strong non-equilibrium flowfield.¹⁸ In addition, though the DSMC method is often regarded as the standard benchmark solution for the numerical simulations of hypersonic rarefied flows, the computational efficiency of the DSMC method is relatively low when simulating the near-continuum flows.

In terms of multi-scale lateral jet flow, the partition calculation is a natural solution, which is not only theoretical but also logical; so to speak, the continuum flow region is computed by NSF equations as the rarefied flow region is solved using the DSMC method.^{19,20} However, two essential issues are often encountered, one is that it is greatly challenging to construct an exact partition standard, and the other is that the statistical fluctuations of the DSMC method occasionally might not be considered for NSF solutions. Consequently, various effective theories and numerical approaches are proposed for the multi-scale flow simulations based on the fundamental Boltzmann equation. These solutions are generally categorized into three groups: (a) mesoscopic algorithms based on the simplified Boltzmann model equations,²¹ such as the discrete velocity method (DVM),^{22,23} unified gas-kinetic scheme (UGKS),²⁴ discrete unified gas kinetic scheme (DUGKS),²⁵ and gas-kinetic unified algorithm (GKUA);²⁶ (b) hybrid methods coupling with hydrodynamic and microscopic descriptions of rarefied flows,²⁷ including the unified gas-kinetic wave-particle method (UGKWP),²⁸ unified stochastic particle method based on the Bhatnagar–Gross–Krook model (USP-BGK),²⁹ general synthetic iterative scheme (GSIS),³⁰ simplified unified wave-particle method (SUWP),³¹ and so on; (c) macroscopic non-Newton–Fourier equations derived via moment methods,³² e.g., Burnett-type equations,³³ Grad’s moment models,³⁴ regularized 13-moment equations (R13),³⁵ etc. In passing, among them, the macroscopic moment models have the

natural potential of favorable calculational efficiency and engineering applications. However, some natural problems still exist to be solved in these above methods, e.g., stochastic fluctuations in particle methods, additional high-order boundary conditions for moment theories, and unaffordable computational costs induced by the velocity space discretization. On the other hand, a series of typical real gas effects such as intensive physical-chemical non-equilibrium processes will occur around the near-space vehicles with a high velocity when the RCS is at work or not.³⁶ Thus, the lack of corresponding solvers against the thermochemical non-equilibrium flows will hinder these methods for further engineering applications of lateral jet interaction with hypersonic thermochemical non-equilibrium crossflow as well.

Independently of the methods aforementioned above, Eu proposed the generalized hydrodynamic equations (GHEs) from a different viewpoint in 1992,³⁷ which is strictly consistent with the second law of thermodynamics. Subsequently, Eu and Myong implemented the adiabatic assumption³⁸ and balance closure³⁹ on GHE and simplified GHE to a nonlinear algebraic system in the physical sense, i.e., nonlinear coupled constitutive relations (NCCR),⁴⁰ which is expected to extend the NSF hydrodynamics into widespread areas. Through a series of typical validation cases about multi-scale non-equilibrium flows,⁴¹ such as one-dimensional shock-wave structure,⁴² Couette flow,⁴³ Poiseuille gas flow,⁴⁴ and three-dimensional complex flow around hypersonic vehicles,⁴⁵ it is demonstrated that NCCR model can not only recover NSF equations in continuum regions^{46,47} but also provide more accurate predictions than NSF equations in rarefied non-equilibrium flows.^{48,49} Additionally, some original studies about NCCR model were carried out and further made this method an efficient and potential tool for solving complex engineering problems of rarefied non-equilibrium flows and hypersonic multi-scale flows, including a discontinuous Galerkin (DG) solver⁵⁰ and a time-dependent computational strategy⁵¹ on unstructured grids, a simplified analytical method⁵² and an undecomposed NCCR algorithm⁵³ in structured finite volume framework, as well as a set of boundary conditions derived from generalized hydrodynamic theory,^{54,55} etc. Later, to reveal the physical mechanism of the coupling effect between the real gas and rarefied gas, this type of method was extended to single-species diatomic and polyatomic gases with non-equilibrium rotational⁵⁶ and vibration modes,⁵⁷ multi-component reacting flows,⁵⁸ along with thermochemical non-equilibrium flows.⁵⁹ Recently, the lateral jet flow problems at different altitudes have been investigated by the NCCR model of calorically perfect gases.⁶⁰ The results showed that the NCCR model predicted accurately the separation zone and flow characteristics near the jet orifice in the continuum-transition regimes; moreover, compared with NSF equations, the NCCR model gave a better agreement with DSMC prediction in describing the complex flow mechanism of shock-wave/shock-wave interaction caused by lateral jet flow.

Following the previous research,⁶¹ this study aims to further investigate the interaction between lateral jet flow with hypersonic rarefied crossflow. Using the newly developed NCCR model of multi-species thermochemical non-equilibrium gases,⁵⁹ the primary objective of this paper is to reveal the physical mechanism underlying lateral jet interaction with hypersonic rarefied crossflow, considering the real gas effect, and to explore the resulting impact on the performance of RCS in an in-flight vehicle. For comparison and to assess the influence of rarefied gas effects on lateral jet interaction in hypersonic flows at high

altitudes, thermochemical non-equilibrium NSF equations are also implemented in this work. It is important to note that this study significantly differs from previous research on the NCCR theory in terms of computational models and research goals. First, the investigation of lateral jet interaction in high-speed crossflows is conducted using the multi-species NCCR model, which accounts for the real gas effect, as opposed to the original NCCR model for calorically perfect gases. Second, this study aims to fill the research gap regarding the performance of RCS at high altitudes in hypersonic thermochemical non-equilibrium flow using the efficient NCCR theory, whereas previous studies focused primarily on accurately describing non-equilibrium flow fields and surface properties around hypersonic vehicles or simply analyzing aerothermodynamic coefficients with the single-species NCCR model. The research examines lateral jet flow conditions, such as the jet pressure ratio and the jet Mach number, at an altitude as high as 80 km. The Terminal High Altitude Area Defense-type (THAAD-type) configuration with a lateral jet is selected as the research subject. To assess the control performance of RCS, the normal force coefficient and jet force/moment amplification factors are utilized as performance indicators.

The remainder of this paper is structured as follows. In Sec. II, a comprehensive mathematical description of the conservation laws and nonlinear thermodynamic relations for multi-species thermochemical non-equilibrium flows is presented, including details on thermochemical kinetic models and transport properties. Section III provides information on the geometric model and computational conditions, while defining three performance indicators for RCS effectiveness. Section IV extensively investigates the influences of different jet pressure ratios and jet Mach numbers on the performance of RCS, following a grid independence analysis. Detailed results, such as complex interaction flowfields and surface pressure distributions, are also presented. Finally, Sec. V summarizes the findings of this study.

II. METHODOLOGY

A. Conservation laws and nonlinear thermodynamic relations for multi-species thermochemical non-equilibrium flows

In general, the validity of the linear thermodynamic relations of Navier–Stokes–Fourier³ is limited up to an altitude of 60 km. However, their applicability at higher altitudes becomes questionable due to the sharp decline in gas density and the increasing dominance of the rarefaction effect. To accurately capture rarefied non-equilibrium phenomena practically and affordably, we employ the conservation laws combined with nonlinear thermodynamic relations, known as the NCCR model, at altitudes exceeding 60 km. The NCCR model is based on Eu’s irreversible thermodynamics theory⁶² and has been extensively demonstrated to effectively describe rarefied gas effects in hypersonic multi-scale flows in numerous published studies.^{57–59,63} Furthermore, in hypersonic flows, the presence of shock-wave structures and the post-shock regions leads to a rapid increase in temperature, resulting in significant thermal and chemical non-equilibrium processes. This complexity necessitates the use of a real gas model to accurately handle thermochemical non-equilibrium effects. Consequently, the conservation equations for single-species gases need to be extended to encompass multi-species gases. Specifically, numerical simulations of thermochemical non-equilibrium flows require the coupling of conservation equations for

species mass, mixture momentum, and total energy, as well as total vibrational-electron-electronic energy conservation equations and chemical reaction kinetic models. In summary, the governing equations of conservation laws for multi-species thermochemical non-equilibrium flows can be expressed as detailed by Zeng *et al.*,⁵⁹

$$\frac{\partial \rho_i}{\partial t} + \nabla \cdot (\rho_i \mathbf{u}) + \nabla \cdot \mathbf{J}_i = \dot{\omega}_i, \quad (1)$$

$$\frac{\partial \rho \mathbf{u}}{\partial t} + \nabla \cdot (\rho \mathbf{u} \mathbf{u} + p \mathbf{I}) + \nabla \cdot (\boldsymbol{\Pi} + \Delta \mathbf{I}) = 0, \quad (2)$$

$$\begin{aligned} \frac{\partial \rho e}{\partial t} + \nabla \cdot [(\rho e + p) \mathbf{u}] + \nabla \cdot \left[(\boldsymbol{\Pi} + \Delta \mathbf{I}) \cdot \mathbf{u} + \mathbf{Q} + \mathbf{Q}_{\text{vib}} - \sum_{i=1}^{\text{ns}} h_i \mathbf{J}_i \right] \\ = 0, \end{aligned} \quad (3)$$

$$\frac{\partial \rho e_{\text{vib}}}{\partial t} + \nabla \cdot (\rho e_{\text{vib}} \mathbf{u}) + \nabla \cdot \left(\mathbf{Q}_{\text{vib}} - \sum_{i=1}^{\text{ns}} e_{\text{vib}}^i \mathbf{J}_i \right) = \dot{\omega}_{\text{vib}}, \quad (4)$$

where ρ_i is the density of species i for $i = 1, 2, \dots, \text{ns}$, and $\rho = \sum_i^{\text{ns}} \rho_i$ stands for the mixture density; p , \mathbf{u} , and t represent the sum of partial pressure of each species, the average velocity vector of mixture gas and time, respectively; $\mathbf{J}_i = -\rho D_i \nabla C_i$ is the diffusion flux, where D_i denotes the diffusion coefficient associated with species i and C_i is the mass fraction of species i ; \mathbf{I} and $\boldsymbol{\Pi}$ denote the unit second-rank tensor and shear stress, respectively; h_i is the species enthalpy; e , e_{vib} , e_{vib}^i , \mathbf{Q} , and \mathbf{Q}_{vib} represent the total energy per unit mass of mixture, total vibrational energy per unit mass of mixture, vibrational energy of species i , heat flux and vibrational heat flux, respectively; $\dot{\omega}_i$ is the source term of the species i , and $\dot{\omega}_{\text{vib}}$ means the vibrational energy source term. Different from the classical NSF equations under Stokes’ hypothesis, the excess normal stress Δ is also considered for completeness, which is associated with the bulk viscosity and rotational effect. Furthermore, according to the work from Kustova *et al.*,⁶⁴ the more accurate shock layer around vehicles and heat transfer to the surface of vehicles were yielded by considering the bulk viscosity effect in the description of hypersonic flows.

It is noteworthy that the NCCR model incorporates the concept of mixed gases through the calculation of the mixture transport coefficient.⁵⁹ In this approach, rather than individually modeling the shear stress, excess normal stress, and heat flux of each species, the total quantities of these non-conserved variables are employed. This decision is both theoretical and logical, considering the computational cost limitations associated with numerical analysis of individual species, given the current constraints on available resources. Consequently, the NCCR model for mixed gases is presented as follows:

$$\boldsymbol{\Pi} q(\kappa) = -2\eta[\nabla \mathbf{u}]^{(2)} - 2\eta \frac{\Delta}{p} [\nabla \mathbf{u}]^{(2)} - 2\eta \frac{1}{p} [\boldsymbol{\Pi} \cdot \nabla \mathbf{u}]^{(2)}, \quad (5)$$

$$\Delta q(\kappa) = -\eta_b \nabla \cdot \mathbf{u} - 3 \frac{\eta_b}{p} (\Delta \mathbf{I} + \boldsymbol{\Pi}) : \nabla \mathbf{u}, \quad (6)$$

$$\mathbf{Q} q(\kappa) = -\lambda \nabla T - \frac{\Delta}{p} \lambda \nabla T - \frac{\boldsymbol{\Pi}}{p} \lambda \nabla T, \quad (7)$$

$$\mathbf{Q}_{\text{vib}} = \lambda_{\text{vib}} \nabla T_{\text{vib}}, \quad (8)$$

where η , η_b , λ , and λ_{vib} represent the shear viscosity, bulk viscosity, thermal conductivity, and vibrational-electron-electronic thermal

conductivity for the mixed gases, respectively; the bracket symbol $[A]^{(2)}$ is the traceless symmetric part of the second-rank tensor A ; T is the translational-rotational temperature; and T_{vib} means the vibrational-electronic temperature. An emphasis is worth placing here that the linear vibrational heat flux similar to the conventional NSF equations is employed to take the thermodynamic non-equilibrium into account in the thermochemical non-equilibrium flows. The non-linear dissipation factor $q(\kappa)$ is obtained as

$$q(\kappa) = \frac{\sinh \kappa}{\kappa}, \quad \kappa = \frac{(mk_B)^{1/4}}{\sqrt{2d}} \cdot \frac{T^{1/4}}{p} \left(\frac{\boldsymbol{\Pi} : \boldsymbol{\Pi}}{2\eta} + \gamma' \frac{\Delta^2}{\eta_b} + \frac{\mathbf{Q} \cdot \mathbf{Q}}{\lambda T} \right)^{1/2}, \quad (9)$$

in which m , d , and k_B mean molecular mass, molecular diameter, and Boltzmann constant, respectively; γ' is equal to $(5 - 3\gamma)/2$, where γ is the specific heat ratio.

For comparison, the linear NSF constitution relations, which are derived through the Chapman–Enskog expansion to first-order, are also written as follows:

$$\boldsymbol{\Pi}_{\text{NSF}} = -2\eta[\nabla \mathbf{u}]^{(2)}, \quad (10)$$

$$\Delta_{\text{NSF}} = -\eta_b \nabla \cdot \mathbf{u}, \quad (11)$$

$$\mathbf{Q}_{\text{NSF}} = -\lambda \nabla T, \quad (12)$$

$$\mathbf{Q}_{\text{vib,NSF}} = \lambda_{\text{vib}} \nabla T_{\text{vib}}. \quad (13)$$

B. Thermochemical non-equilibrium models and transport properties

As is well known, a chemical kinetic model is an integral part of the numerical simulations for hypersonic thermochemical non-equilibrium flows. In this work, Gupta’s chemical reaction model for five species is utilized,⁶⁵ which includes six reaction formulas. The rate constants of the forward $k_{f,r}$ and backward $k_{b,r}$ for the reaction r are calculated by the classical Arrhenius law as⁶⁶

$$k_{f,r} = A_{f,r} T_c^{B_{f,r}} \exp\left(-\frac{E_{f,r}}{T_c}\right), \quad k_{b,r} = A_{b,r} T_c^{B_{b,r}} \exp\left(-\frac{E_{b,r}}{T_c}\right), \quad (14)$$

where $A_{f,r}$, $A_{b,r}$, $B_{f,r}$, $B_{b,r}$, $E_{f,r}$, and $E_{b,r}$ are the reaction rate coefficients and are given in Table I. The controlling temperature $T_c = T^a T_{\text{vib}}^b$ for the chemical reaction rates is given by Park’s two-temperature model,⁶⁷ where a and $b = 1 - a$ are the exponential weight factors of translational-rotational and vibrational-electronic temperature and indicate the contribution of each temperature mode on a specific chemical reaction. Specifically, in this paper, $a = b = 0.5$ is assumed

for the dissociation reaction, while $a = 1$, $b = 0$ is set to the neutral exchange reaction and recombination reaction.

The mass production rate per unit volume $\dot{\omega}_i$ of species i is computed by the following equation according to the law of mass reaction:⁶⁸

$$\dot{\omega}_i = M_i \sum_{r=1}^{\text{nr}} (v'_{ri} - v_{ri}) \left[k_{f,r} \prod_{i=1}^{\text{ns}} \left(\frac{\rho_i}{M_i} \right)^{v_{ri}} - k_{b,r} \prod_{i=1}^{\text{ns}} \left(\frac{\rho_i}{M_i} \right)^{v'_{ri}} \right], \quad (15)$$

where nr is the number of total chemical reactions and ns is the number of species; v_{ri} and v'_{ri} are the stoichiometric coefficient of products and reactants of specie i in reaction r , respectively.

In terms of the vibrational energy source term in Eq. (4), the vibrational-electron-electronic energy conservation equation is under the assumption that all molecular species are represented by one vibrational-electronic temperature, and the simplified form of the vibrational energy relaxation term implemented in this study can be decomposed into two parts as follows:

$$\dot{\omega}_{\text{vib}} = \Omega_{\text{CV}} + \Omega_{\text{TV}} = \sum_{i \in \text{molecule}} \dot{\omega}_i e_{\text{vib}}^i + \rho \frac{e_{\text{vib}}^*(T) - e_{\text{vib}}(T_{\text{vib}})}{\tau_{\text{vib}}}, \quad (16)$$

in which Ω_{CV} stands for the vibrational energy change due to a chemical reaction, Ω_{TV} denotes the exchange of energy between translational and vibrational modes of molecules as well as it is dictated by the Landau–Teller model, and τ_{vib} is the modified vibrational relaxation time.⁷⁰

The computation of mixture transport properties is conducted through Wilke’s semi-empirical mixing rule,⁷¹ for instance, total viscosity and thermal conductivity. Therein, species viscosities are calculated by Gupta’s curve fit,⁷² and species thermal conductivities are modeled by the modified Eucken’s relation.⁷³ The expression of species viscosities η_i is given as

$$\eta_i = \exp[(A_i \ln T_{\text{local}} + B_i) \ln T_{\text{local}} + C_i]. \quad (17)$$

Here, T_{local} is the local temperature; A_i , B_i , and C_i are the constants for the viscosity curve fits of species i , and the values are given in Table II.

Since the bulk viscosity is not necessary to be considered for monatomic gases and the viscosity coefficient ratio $f_b = \eta_b/\eta$ of different diatomic gases is not identical, the bulk viscosity η_b of mixed gases is corrected as follows:

$$\eta_b = \eta \cdot \sum_{i=\text{dia}} \chi_i \cdot f_b, \quad (18)$$

TABLE I. Arrhenius forward/backward reaction rate coefficients for five-species air model (Gupta’s model).

Reaction	$A_{f,r}(\text{cm}^3/\text{mol} \cdot \text{s})$	$B_{f,r}$	$E_{f,r}(\text{K})$	$A_{b,r}(\text{cm}^3/\text{mol} \cdot \text{s})$	$B_{b,r}$	$E_{b,r}(\text{K})$
$\text{O}_2 + \text{M}_1 \rightleftharpoons 2\text{O} + \text{M}_1$	3.61×10^{18}	-1.0	5.94×10^4	3.01×10^{15}	-0.5	0
$\text{N}_2 + \text{M}_2 \rightleftharpoons 2\text{N} + \text{M}_2$	1.92×10^{17}	-0.5	1.131×10^5	1.09×10^{16}	-0.5	0
$\text{N}_2 + \text{N} \rightleftharpoons 2\text{N} + \text{N}$	4.15×10^{22}	-1.5	1.131×10^5	2.32×10^{21}	-1.5	0
$\text{NO} + \text{M}_3 \rightleftharpoons \text{N} + \text{O} + \text{M}_3$	3.97×10^{20}	-1.5	7.56×10^4	1.01×10^{20}	-1.5	0
$\text{NO} + \text{O} \rightleftharpoons \text{O}_2 + \text{N}$	3.18×10^9	1	1.97×10^4	9.63×10^{11}	0.5	3.6×10^3
$\text{N}_2 + \text{O} \rightleftharpoons \text{NO} + \text{N}$	6.75×10^{13}	0	3.75×10^4	1.5×10^{13}	0	0

TABLE II. Constants for viscosity curve fits (Gupta's model).

Species	A_i	B_i	C_i
O	0.0205	0.4257	-11.5803
N	0.0120	0.5930	-12.3805
O ₂	0.0484	-0.1455	-8.9231
N ₂	0.0203	0.4329	-11.8153
NO	0.0452	-0.0609	-9.4596

where χ_i stands for the species molar fraction and $\sum_{i=\text{dia}} \chi_i$ is the sum of molar fractions of all diatomic gases; as suggested by Myong,⁷⁴ the viscosity coefficient ratio f_b is supposed as 0.8 in this study for simplification.

In addition, the effective diffusion coefficients D_i are computed by a simplified expression as follows:

$$\rho D_i = \frac{\eta}{Sc} \frac{1 - C_i}{1 - \chi_i}, \tag{19}$$

in which C_i is the mass fraction of species i , and the Schmidt number Sc is assumed as 0.25 for neutral species.

III. PROBLEM DESCRIPTION

A. Geometric model and computational conditions

The computational model employed in this study corresponds to the THAAD-type configuration with a lateral jet, which aligns with the model utilized in the study by Zhuang *et al.*⁵ The geometric details and specific dimensions are visually presented in Fig. 1. The overall length of the model is 483.75 mm, while the diameter of the bottom base measures 92.50 mm. The circular jet orifice is situated on the flare skirt section, precisely 216.25 mm away from the nose.

The lateral jet and incoming crossflow conditions for the THAAD-type model are provided in Table III. The freestream Mach number is set to 20, corresponding to a flight altitude of 80 km. At this altitude, the slip-transition region is encountered, rendering the traditional NSF equations inadequate for accurately predicting the hypersonic vehicle's

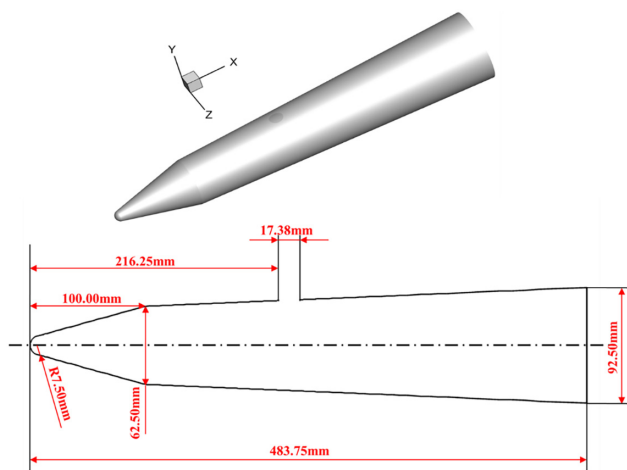


FIG. 1. Geometry and specific dimensions of the THAAD-type model.

TABLE III. Computational conditions of the THAAD-type model.

Parameter or impact factor	Value
Flight altitude (km)	80
Freestream Mach number	20
Freestream pressure (Pa)	1.052 47
Freestream temperature (K)	198.639
Jet temperature (K)	300
Wall temperature (K)	300
Angle of attack (deg)	0
Angle of sideslip (deg)	0
Jet pressure ratio	50, 100, 150, 200, 250, 300
Jet Mach number	2, 2.5, 3, 3.5, 4

aerodynamics and aero-heating data. The lateral jet flow has a static temperature of 300 K. For the wall boundary conditions, a completely non-catalytic and isothermal setting is employed, maintaining a constant temperature of 300 K. The interaction between the gas flow and solid wall follows the first-order Maxwell-Smoluchowski (M/S) slip and jump boundary conditions, which utilize full tangential momentum and thermal accommodation coefficients.

Both the freestream gas and lateral jet gas consist of air, with mass fractions of 78% N₂ and 22% O₂, respectively. The jet pressure ratio (PR) denotes the ratio of the lateral jet static pressure to the static pressure of the incoming crossflow. In this work, the Gupta's five-species chemical kinetic model, coupled with Park's two-temperature model as mentioned earlier, is employed. Similar to the reference study,⁵ two key factors are investigated: the jet pressure ratio and the jet Mach number. For the standard case, an angle of attack of 0 deg, an angle of sideslip of 0 deg, a jet pressure ratio of 100, and a jet Mach number of 3 are selected. It is important to note that when studying one impact factor, the other impact factors are assumed to be the same as those in the standard case.

B. Performance indicators for the efficiency of the reaction control system

The complex interaction between the lateral jet flow and crossflow significantly influences the pressure distributions on the surface, consequently modifying the aerodynamic characteristics of the THAAD-type model. For each case involving the aforementioned impact factors, two types of simulations are conducted: one with the lateral jet activated and the other with the lateral jet deactivated. The latter, serving as a reference case, solely provides the aerodynamic force on the THAAD-type model in the absence of the lateral jet. Regarding the lateral jet interaction problem, the total force acting on the THAAD-type model is typically decomposed into three components: the aerodynamic force without lateral jet, the force resulting from the interaction between the lateral jet flow and the incoming crossflow, and the thrust force induced by the lateral jet. To assess the impact of this interaction on the control forces and moments, the jet amplification factor is commonly utilized. However, it is important to note that the expression of the force/moment amplification factors varies across different literature sources.^{4,5,17} Therefore, in this study, three metrics are defined to evaluate the control efficiency of RCS. These metrics

include the normal force coefficient C_N , the force amplification factor K_F , and the moment amplification factor K_M . Their formulations are presented as follows:

$$C_N = \frac{F_{jet_on} + T_{jet}}{(1/2)\rho_\infty v_\infty^2 S_f}, \quad (20)$$

$$K_F = 1 + \frac{F_{jet_on} - F_{jet_off}}{T_{jet}}, \quad (21)$$

$$K_M = 1 + \frac{M_{jet_on} - M_{jet_off}}{M_{jet}}, \quad (22)$$

$$T_{jet} = S_{jet}(p_{jet} - p_\infty + \rho_{jet}v_{jet}^2), \quad M_{jet} = T_{jet} \cdot l, \quad (23)$$

where the subscripts “jet” and “ ∞ ” denote the parameter of lateral jet and incoming crossflow, respectively. v stands for the velocity, ρ represents the density, and p is the static pressure. S_f is the bottom base area of the THAAD-type model, and l is the moment arm of the thrust to the reference point, i.e., the nose of the THAAD-type model. F_{jet_on} and F_{jet_off} indicate the aerodynamic force when the lateral jet is on and off, respectively. Likewise, M_{jet_on} represents the moment generated with the lateral jet on, and M_{jet_off} denotes the moment produced with the lateral jet off. T_{jet} is the thrust force induced by the lateral jet, and M_{jet} means the moment induced by the lateral jet thrust. By these three indicators defined above, the control performance of RCS can be evaluated. One more thing should be stated here that the force/moment amplification factor greater than 1 indicates a favorable interaction between the lateral jet flow and incoming crossflow, so to speak, the lateral jet enhances the control performance of RCS. Otherwise, the force/moment amplification factor less than 1 means that the lateral jet interaction has adverse effects on the control performance.

IV. RESULTS AND DISCUSSION

The first two sections of this paper provide a comprehensive description of the numerical method, study object, and computational conditions employed in this study. In this section, the focus shifts to conducting numerical simulations of hypersonic thermochemical non-equilibrium flow over the THAAD-type model equipped with a lateral jet at an altitude of 80 km under various lateral jet flow conditions, utilizing the thermochemical non-equilibrium NCCR theory. Subsequently, a detailed analysis is performed to examine the flow mechanism of lateral jet interaction with hypersonic crossflow, with particular attention given to understanding how the two impact factors, namely, the jet pressure ratio and the jet Mach number, influence the performance of RCS. Before delving into the detailed analysis of the numerical results, a grid independence study is systematically conducted to ensure that the computational grids do not unduly influence the outcomes. Importantly, it should be noted that our recent studies, as documented in the published literature, have already examined and demonstrated the physical consistency and accuracy of the thermochemical non-equilibrium NCCR model in hypersonic rarefied flows or high-altitude reverse jet flows, considering the real gas effect. Specifically, the results obtained using the thermochemical non-equilibrium NCCR model^{59,61} exhibits better agreement with DSMC simulations or flight data than those derived from the conventional NSF equations in strongly non-equilibrium regions. These results encompass surface property distributions, contours of physical quantities, and distributions of various components within the flowfield.

A. Grid independence

To get rid of the influence of the grid on the numerical simulation results, a grid independence analysis is performed for the thermochemical non-equilibrium NCCR model with four levels of grid refined, i.e., grid points in normal, circumferential, and flow directions: Grid A ($51 \times 121 \times 197$), Grid B ($81 \times 121 \times 197$), Grid C ($101 \times 121 \times 197$), and Grid D ($121 \times 121 \times 197$). All the structured grids are constructed with normal spacing of 1×10^{-4} m on the surface to pledge that the cell Reynolds number meets the accurate numerical demand. Specifically, the requirements for aerodynamics/aero-heating converges and tested aerodynamics/aero-heating predictions can be rightly attained with $Re_{cell} \in (0, 1)$, which is confirmed through many numerical tests.^{58,75} Moreover, special attention is given to the grid distribution in the vicinity of the jet orifice to ensure the generation of physically reliable numerical results. As illustrated in Fig. 2, the grids designated as C and D, which have been refined, yield nearly identical solutions. In contrast, the coarser grids A and B exhibit noticeable deviations in the distributions of Mach number. Consequently, the refined grid C, encompassing approximately 2.85×10^6 cells, meets the criteria for grid independence and is selected as a suitable compromise between computational cost and numerical accuracy for conducting further investigations in this study.

B. Detailed flowfield of lateral jet interaction

In hypersonic rarefied flow considering the real gas effect, the interaction between high-pressure lateral jet flow and high-speed crossflow gives rise to intricate lateral jet interaction phenomena. Figure 3 provides a comprehensive visualization of the three-dimensional complex flowfield structure induced by the interaction between the lateral jet flow and hypersonic thermochemical non-equilibrium flows, as computed by the NCCR model under the condition of $PR = 300$, $Ma = 3$. The surface pressure contours and streamline distributions are shown on the surface of the THAAD-type

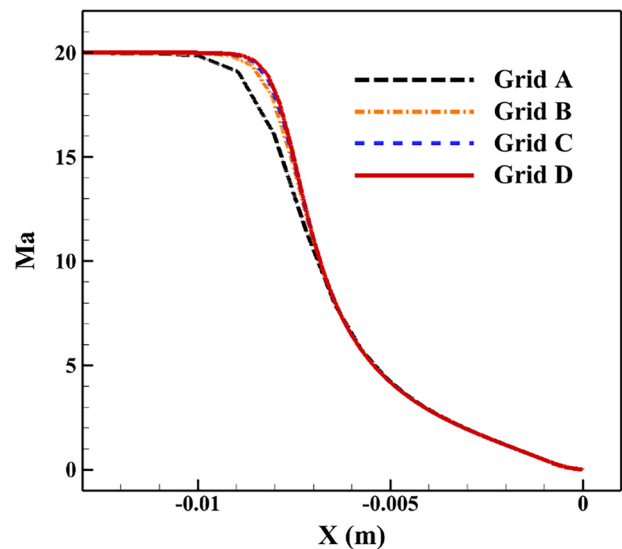


FIG. 2. Mach number distributions for four different grid resolutions along the stagnation line.

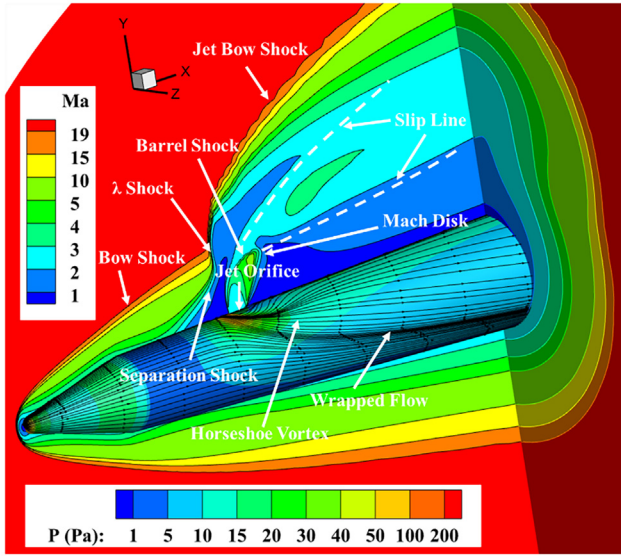


FIG. 3. Three-dimensional flowfield structures of the THAAD-type model with a lateral jet computed by NCCR model (PR = 300, Ma = 3).

model, while the Mach number profile is presented on the symmetric plane ($Z = 0$) of the computational domain. Due to the significant difference in pressure between the lateral jet flow and the rarefied incoming crossflow, the highly under-expanded lateral jet flow acts as a barrier to the crossflow, resulting in the formation of an inclined barrel shock around the jet orifice and the termination of expansion at the Mach disk. The Mach disk, essentially a normal shock, decelerates the lateral jet flow inside the barrel shock and forms a slip surface with the hypersonic incoming crossflow around and over the barrel shock downstream. It is worth noting that both the barrel shock and the Mach disk exhibit unsteady behavior, possibly attributed to acoustic waves propagating through the jet orifice.² The blockage caused by the barrel shock leads to the generation of a detached jet bow shock upstream of the injection point, which, in turn, induces a wedge-like region of separated flow ahead of the injection due to the adverse pressure gradient resulting from the shock wave/boundary-layer interaction between the jet bow shock and the boundary layer of the incoming crossflow. This separated region lifts the crossflow boundary layer and generates a series of compression waves that merge into a separation shock in its vicinity. The separation shock, the bow shock at the nose of the THAAD-type model, and the jet bow shock collectively contribute to the formation of a shock wave structure, as frequently discussed in the literature.^{9,76} Furthermore, counter-rotating horseshoe vortices are generated in the flow separation region in front of the jet orifice. These vortices wraparound the lateral jet and subsequently travel downstream along the surface. The characteristic flow structure, as depicted in Fig. 3, bears resemblance to that of a lateral jet ejecting from a flat plate. Previous studies by Champigny and Lacau⁷⁷ have summarized widely accepted flowfield structures for a lateral jet injecting into a supersonic crossflow over a flat plate. However, subsequent investigations by Brandeis *et al.*¹⁰ have revealed significant discrepancies between a flat plate and a body of revolution in terms of flowfield structures during lateral jet interaction, particularly the jet wraparound

effect. Specifically, the separated flow ahead of the jet orifice wraps over the body from the upper surface to the lower surface, forming the wrapped flow and altering the local pressure of the crossflow on the opposite side of the jet orifice, as illustrated in Fig. 3. The aforementioned complex flowfield structures, which are crucial in the context of lateral jet interaction, are effectively captured through the numerical simulations conducted in this study. This successful reproduction underscores the engineering potential of the NCCR theory, including the present thermochemical non-equilibrium NCCR model, for analyzing complex lateral jet flows of this nature.

Figure 4 illustrates the predicted surface streamlines and pressure contours near the jet orifice using the NCCR model. Upstream of the jet orifice, a separated flow circulates, leading to an increase in pressure and the formation of a high-pressure region on the surface. Conversely, a low-pressure region is observed downstream of the injection. This low-pressure region, as hypothesized by Viti *et al.*,⁷⁸ arises not only from the blockage of the barrel shock but also from the downstream movement of surface trailing vortices. The high-pressure region positively contributes to the generation of a downward force resulting from lateral jet interaction. Conversely, the low-pressure region behind the lateral jet induces an upward interaction force. The recirculation zone, clearly annotated in Fig. 5, plays a significant role in generating a nose-down interaction moment for the THAAD-type model. The interaction between the horseshoe vortices, the jet wraparound effect, and the crossflow boundary layer can further modify the resultant interaction forces and moments on the THAAD-type model, ultimately impacting the control performance of the lateral jet. Understanding the lateral jet interaction is thus crucial for predicting the aerodynamic characteristics of vehicles and improving the control efficiency of RCS. Furthermore, Fig. 4 reveals that after the incoming crossflow passes through the separation zone within the boundary layer, it undergoes two successive expansion processes.⁷⁹ The first is the reattachment expansion, which occurs as the crossflow traverses the separation region and encounters the jet orifice. The second is the lateral expansion that occurs as the crossflow circumvents the barrel shock. Subsequently, the crossflow reaches the reattachment point before encountering the reflected shock or recompression shock, as indicated in Fig. 6.

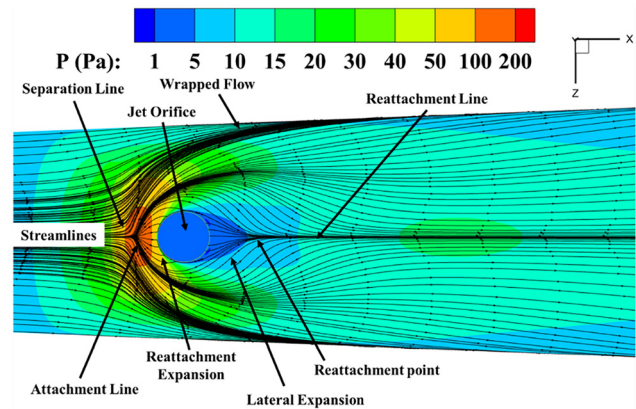


FIG. 4. Surface streamlines near the jet orifice calculated by the NCCR model (PR = 300, Ma = 3).

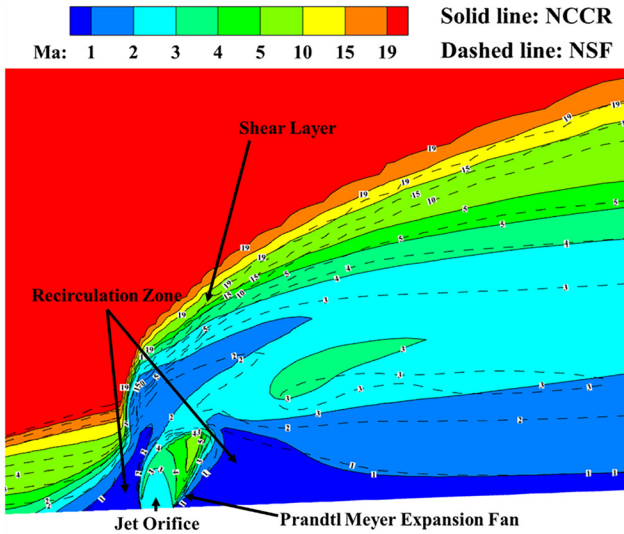


FIG. 5. Mach number contours on the symmetry plane ($Z = 0$) simulated by NSF equations and NCCR model ($PR = 300$, $Ma = 3$).

To investigate the impact of the rarefied gas effect on the intricate flowfield associated with lateral jet interaction, the contours of Mach number and pressure on the symmetry plane ($Z = 0$) are presented in Figs. 5 and 6, respectively. The simulations are performed using both the NSF equations and the NCCR model. As observed in Figs. 5 and 6, the lateral jet flow undergoes a Prandtl–Meyer expansion fan upon exiting the jet orifice and attempts to penetrate the low-pressure crossflow, resulting in the formation of a high-pressure zone near the λ -shock wave structure due to the interactions between shock waves. Additionally, a high-speed shear layer is generated between the ambient crossflow and the lateral jet flow. A comparison between the

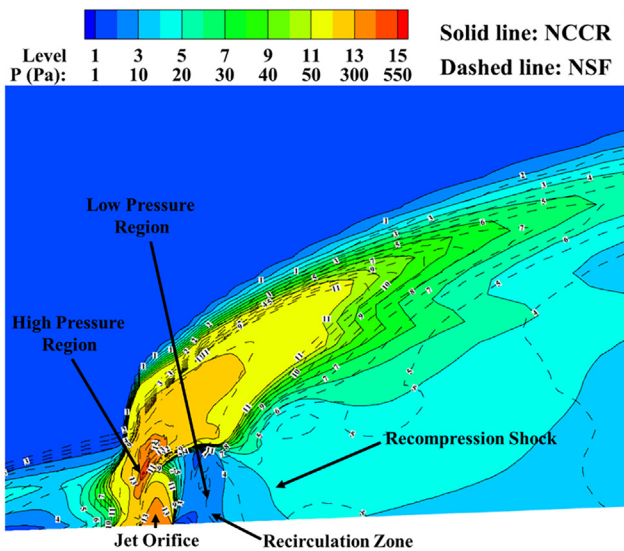


FIG. 6. Pressure contours on the symmetry plane ($Z = 0$) simulated by NSF equations and NCCR model ($PR = 300$, $Ma = 3$).

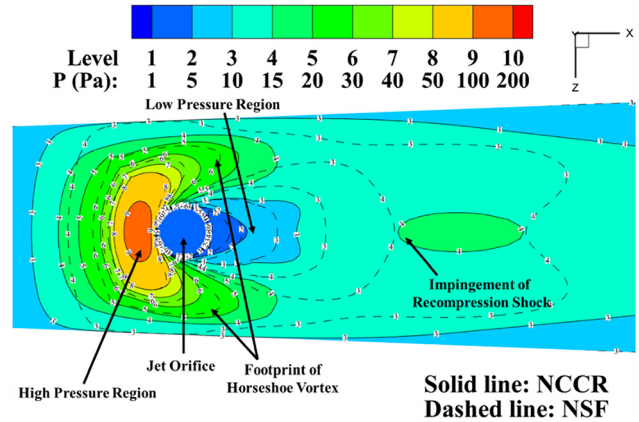


FIG. 7. Surface pressure distributions near the jet orifice predicted by NSF equations and NCCR model ($PR = 300$, $Ma = 3$).

flowfield obtained using the NCCR model and the NSF equations reveals two conspicuous discrepancies attributed to the rarefied gas effect. First, the penetration height of the high-pressure lateral jet flow into the low-pressure crossflow is greater in the NCCR model compared to the NSF equations. Second, the high-speed shear layer is weaker in the NCCR model than in the NSF equations. Figure 7 presents the surface pressure distributions near the jet orifice as predicted by the NSF equations and the NCCR model. It is evident that both the extent of the high-pressure region ahead of the jet orifice and the low-pressure region behind the jet orifice are larger in the NCCR model than in the NSF equations. This observation indicates that the rarefied gas effect can attenuate the compressibility of the barrel shock and the expansibility of the Prandtl–Meyer expansion fan, consistent with previous studies.^{48,50} Furthermore, it is worth noting, as mentioned by Anderson,⁶⁹ that the real gas effect can enhance the compressibility of strong shock waves and the intensity of expansion waves.

For a more comprehensive comparison, Fig. 8 presents the surface pressure coefficients on the symmetry plane ($Z = 0$) calculated using both the NSF equations and the NCCR model. Two simulations

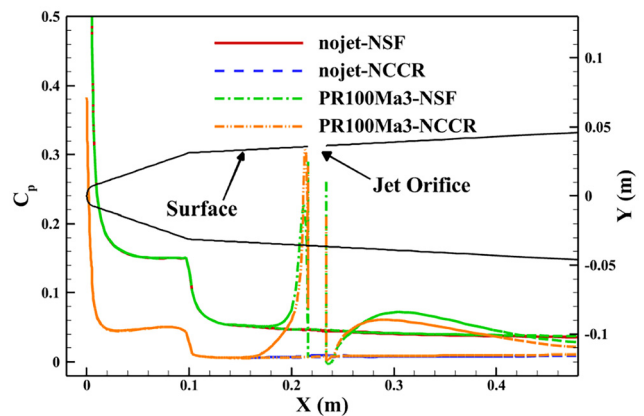


FIG. 8. Comparison of surface pressure coefficients on the symmetry plane ($Z = 0$) computed by NSF equations and NCCR model with jet-on and jet-off.

08 April 2024 03:59:57

are conducted: one involving a lateral jet and the other without, where the latter serves as the reference case for thorough analysis. The primary influence of lateral jet interaction with high-speed crossflow is observed in the regions preceding and trailing the jet orifice, while the pressure distributions on the lower surface remain largely unaffected by the lateral jet flow. Specifically, the pressure exhibits a sharp increase upstream of the injection, followed by a decrease and gradual enlargement downstream of the injection. Notably, the affected region of pressure distributions ahead of the jet orifice, as computed by the NCCR model, is larger than that obtained from the NSF solution due to the rarefied gas effect. However, the peak pressure value near the jet orifice, calculated by the NCCR model, aligns well with the NSF equations. It is important to acknowledge that the high-speed crossflow represents a rarefied flow, while the flows in the injection region fall within the continuum regime. Moving downstream of the lateral jet flow, the affected region of pressure distributions, as predicted by the NCCR model, is also larger than that derived from the NSF equations. Furthermore, the peak pressure value computed by the NCCR model is lower than that obtained from the NSF equations, both of which are typical characteristics resulting from the rarefied gas effect. Overall, the NCCR model accurately captures the rarefied gas effect in the intricate lateral jet interaction at high altitudes while recovering the NSF solution within the continuum regime. In Fig. 9, the surface pressure coefficients on the axial plane ($X = 0.22494\text{m}$) are compared between the NSF equations and the NCCR model. The NCCR model predicts a more pronounced jet wrap-around effect compared to the NSF solution. This finding suggests that the rarefied gas effect may intensify the jet wrap-around effect, subsequently influencing the control efficiency of RCS.

C. Influence of jet pressure ratio

In Secs. IV A and IV B, we conducted a comprehensive analysis and discussion of the intricate flowfield resulting from lateral jet

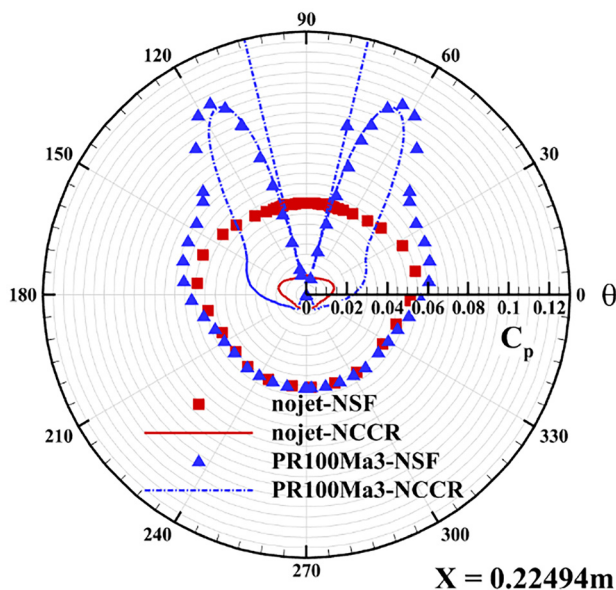


FIG. 9. Comparison of surface pressure coefficients on the axial plane ($X = 0.22494\text{ m}$) predicted by NSF equations and NCCR model with jet-on and jet-off.

interaction with hypersonic thermochemical non-equilibrium flow. Furthermore, we elaborated on the influence of the rarefied gas effect on the complex flowfield structures arising from lateral jet interaction, employing the results obtained from the NCCR model and the NSF solution. It is widely recognized that the interaction between lateral jet flow and hypersonic crossflow significantly alters the pressure distribution on the surface of the vehicles, thereby impacting the aerodynamic characteristics of the vehicles and the control efficiency of RCS. Regarding the control force generated by lateral jet flow, two aspects should be taken into consideration. First, direct control force originates from the lateral jet thrust, while the second aspect arises from the intricate interaction between lateral jet flow and the incoming crossflow. The latter aspect is closely associated with the flowfield structures and primarily manifests in the variations of surface pressure. Based on the flowfield characteristics outlined in Figs. 3–7, four types of affected surface pressure resulting from lateral jet interaction have been identified.⁸⁰ These include surface pressure in the flow separation region located ahead of the jet orifice, surface pressure in the low-pressure region situated behind the jet orifice, surface pressure influenced by the jet wrap-around effect, and surface pressure attributable to shock recovery further downstream. To evaluate the extent of lateral jet interaction, performance indicators or jet amplification factors for the control efficiency of RCS are commonly employed, as defined in Eqs. (20)–(22) according to relevant literature. To achieve effective vehicle operation, two preferred approaches for modifying the control force and moment are through the manipulation of the jet pressure ratio (PR) and the jet Mach number. Consequently, Secs. IV C and IV D explore the impact of these two influencing factors on the performance of RCS. Furthermore, it is worth noting that the distinct characteristics observed in comparison to simulation results in the continuum region primarily stem from the rarefied gas effect induced by high altitudes and the real gas effect resulting from hypersonic flows.

Regarding the impact of the jet pressure ratio, we now proceed with the analysis by examining the force/moment amplification factors. Figure 10 illustrates the variations of K_F , K_M , and concerning the jet pressure ratio, as computed using both the NSF equations and the NCCR model. The range of jet pressure ratios considered in this study spans from 50 to 300. As evident from Fig. 10, both the force and moment amplification factors, obtained from both the NSF solution and the NCCR algorithm, exhibit a gradual decrease as the jet pressure ratio increases. This declining trend aligns with the findings presented in a previous study using the NSF equations,⁸ as well as numerical simulations conducted via the DSMC method,⁵ and indirectly indicated by an empirical formula proposed by Roger.⁸¹ Although the force/moment amplification factors are greater than 1 under the specified computational conditions, it is important to emphasize that the positive gain effect on enhancing the RCS's performance diminishes and may even reverse as the jet pressure ratio turns higher, due to the decreasing values of the force/moment amplification factors. Additionally, the absolute value of the normal force coefficient, calculated using both methods, exhibits an almost linear increase as the jet pressure ratio grows larger. Notably, this trend closely resembles the results obtained from the DSMC method.⁵ Figure 10 includes a specific comparison between the results obtained from the NCCR model and those derived from the NSF equations. This analysis indirectly sheds light on the influence of the rarefied gas effect on the control efficiency of RCS. In other words, at high altitudes characterized by low density,

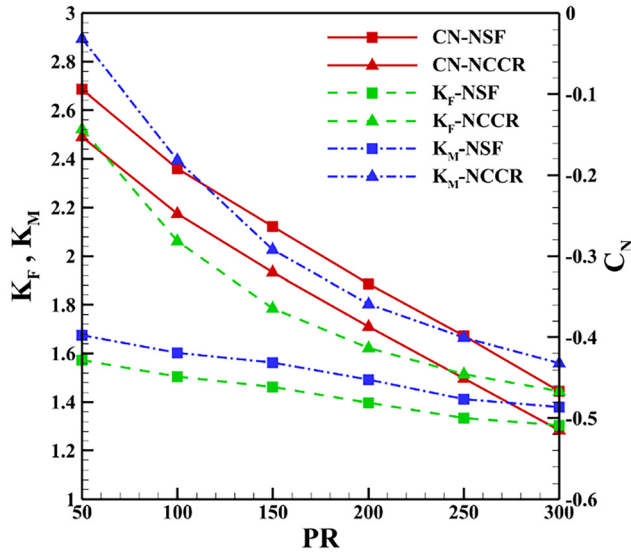


FIG. 10. The variation of K_F , K_M , and C_N with the jet pressure ratio computed by NSF equations and NCCR model.

the numerical simulations based on the NSF equations tend to underestimate the control efficiency of RCS. Moreover, the degree of underestimation diminishes with an increasing jet pressure ratio. These findings underscore the significance of employing an accurate and efficient approach, such as the NCCR model proposed in this study, for numerical simulations of lateral jet interaction in high-altitude scenarios, considering the real gas effect.

To gain further insight into the variations of these force/moment amplification factors, our focus turns to the distribution of surface pressure coefficients on the THAAD-type model. Figure 11 showcases the local distributions of surface pressure coefficients on the symmetry plane ($Z = 0$) as predicted by the NCCR model, considering different jet pressure ratios. It is evident that as the jet pressure ratio increases from 50 to 300, a larger high-pressure zone emerges ahead of the jet

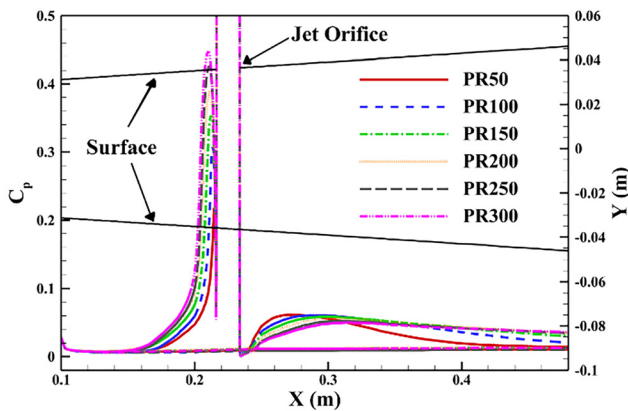


FIG. 11. Local distributions of surface pressure coefficients predicted by NCCR model on the symmetry plane ($Z = 0$) with different jet pressure ratios.

orifice, accompanied by a larger low-pressure zone appearing aft of the jet orifice. Furthermore, the altered region of surface pressure further downstream exhibits a greater extent of change. These zones, influenced by lateral jet interaction, collectively contribute to the decrease in the moment amplification factor. Moreover, for smaller jet pressure ratios, the location of the peak value of the surface pressure coefficient, whether ahead or aft of the jet orifice, is closer to the jet orifice. In the case of the jet wraparound effect, Fig. 12 presents the distribution of surface pressure coefficients on the axial plane ($X = 0.22494\text{m}$) as predicted by the NCCR model, considering different jet pressure ratios. It is evident that as the jet pressure ratio increases, a more pronounced jet wraparound effect becomes apparent. This observation aligns with findings reported in a previous study by Nunn.⁸² Furthermore, due to the additional negative impact of the jet wraparound effect, the force amplification factor experiences a decline, and this decline occurs at a faster rate than that observed for the moment amplification factor as the jet pressure ratio increases.

D. Influence of jet Mach number

We now shift our attention to examining how the jet Mach number influences the force/moment amplification factors. As illustrated in Fig. 13, both the force and moment amplification factors exhibit a decreasing trend as the jet Mach number increases from 2 to 4. Conversely, the absolute value of the normal force coefficient shows an increasing trend. These trends align with those observed for the jet pressure ratio, and similar findings have been reported in previous studies.^{5,83} It is important to note that as the jet Mach number becomes higher, the force/moment amplification factors may fall below 1, indicating a reduction and potential reversal of the positive gain effect on enhancing the RCS's performance. Additionally, the rarified gas effect captured by the NCCR model, in comparison to the

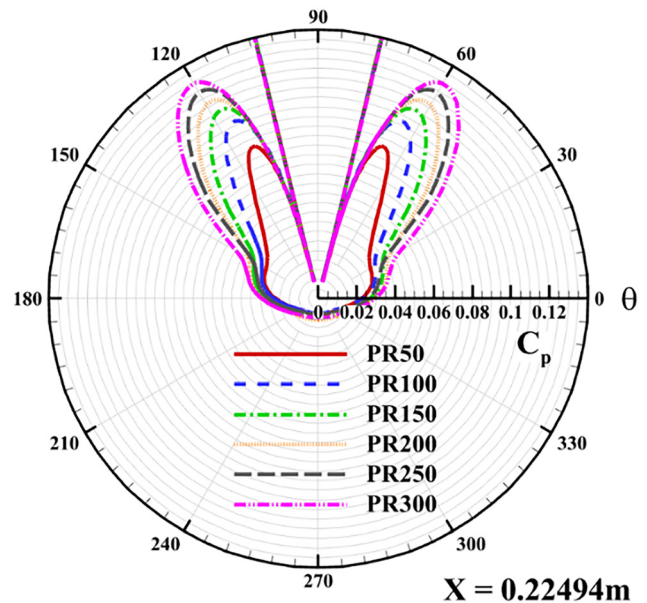


FIG. 12. Distributions of surface pressure coefficients simulated by NCCR model on the axial plane ($X = 0.22494\text{m}$) with different jet pressure ratios.

08 April 2024 03:59:57

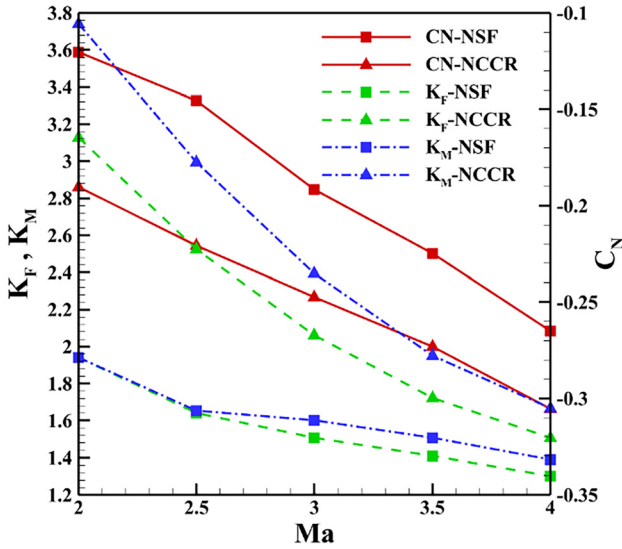


FIG. 13. The variation of K_F , K_M , and C_N with the jet Mach number computed by NSF equations and NCCR model.

NSF solution, has a significant impact on the force/moment amplification factors. Notably, the degree of this impact diminishes as the jet Mach number increases.

Similarly, we investigate the surface pressure distributions to conduct a detailed analysis. Figure 14 showcases the local distributions of surface pressure coefficients computed using the NCCR model on the symmetry plane ($Z = 0$) considering various jet Mach numbers. It is evident that as the jet Mach number increases, both the interaction regions ahead and aft of the jet orifice expand, while the peak value of the surface pressure coefficient ahead or aft of the jet orifice decreases. Similar to the jet pressure ratio, an increase in the jet Mach number leads to the peak value of the surface pressure coefficient occurring closer to the jet orifice. Furthermore, Fig. 15 displays the distributions of surface pressure coefficients obtained from the NCCR model on the axial plane ($X = 0.22494$ m) for different jet Mach numbers.

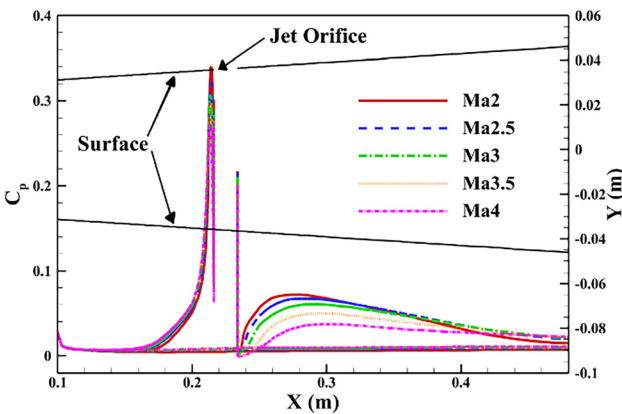


FIG. 14. Local distributions of surface pressure coefficients predicted by NCCR model on the symmetry plane ($Z = 0$) with different jet Mach numbers.

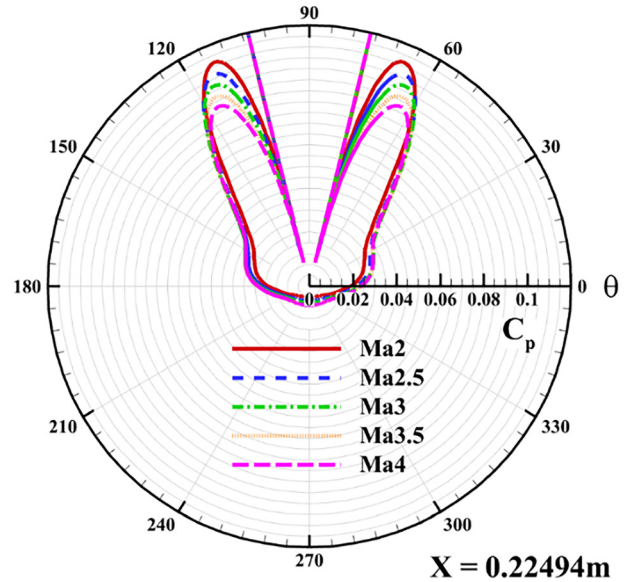


FIG. 15. Distributions of surface pressure coefficients simulated by NCCR model on the axial plane ($X = 0.22494$ m) with different jet Mach numbers.

The results indicate that the influence of the jet Mach number on the jet wraparound effect is not significant under the simulated conditions.

V. CONCLUDING REMARKS

This paper presents numerical simulations of lateral jet interaction in hypersonic thermochemical non-equilibrium crossflows using the recently developed thermochemical non-equilibrium NCCR model. A grid independence analysis was performed to ensure the reliability of the computational results. These results enabled a detailed analysis of the flow mechanism of lateral jet interaction in hypersonic rarefied crossflows considering the real gas effect through the examination of complex interaction flowfield characteristics and surface pressure distributions. A particular focus was placed on investigating the impact of two key factors, namely, the jet pressure ratio and the jet Mach number, on the performance of the reaction control system (RCS) of an in-flight vehicle. The numerical results and corresponding analyses led to the following conclusions:

- (1) The thermochemical non-equilibrium NCCR model satisfactorily reproduced the intricate flowfield structures associated with lateral jet interaction at high altitudes. This indicates the engineering potential of the NCCR theory for modeling complex lateral jet flows in hypersonic rarefied flows while considering the real gas effect.
- (2) A comparison between the flowfield computed using the NCCR model and the NSF equations revealed notable discrepancies induced by the rarefied gas effect. These discrepancies include a greater penetration height of the lateral jet flow into the incoming crossflow and the presence of a weaker high-speed shear layer near the jet orifice. Additionally, the rarefied gas effect weakened the compressibility of the barrel shock and the expansibility of the Prandtl-Meyer expansion fan, while strengthening

the jet wraparound effect. Consequently, the rarefied gas effect had a discernible impact on the control efficiency of RCS.

- (3) As the jet pressure ratio or the jet Mach number increased, both the force and moment amplification factors decreased, while the absolute value of the normal force coefficient increased. Furthermore, the study investigated the influence of the rarefied gas effect on the RCS's performance. The results indicated that the rarefied gas effect, as captured by the NCCR model compared to the NSF solution, had a significant impact on the force/moment amplification factors. The degree of the impact decreased as the jet Mach number or the jet pressure ratio increased.

In summary, it is vital to employ an accurate and efficient method, such as the proposed NCCR theory, for conducting numerical simulations of lateral jet interaction in hypersonic thermochemical non-equilibrium flows at high altitudes. The findings of this study provide valuable insight into the complex flow behavior and the implications for the performance of RCS, contributing to the advancement of research in hypersonic aerodynamics.

ACKNOWLEDGMENTS

The research was financially supported by the National Natural Science Foundation of China (Grant Nos. 92271114, 92271204, 12002306, and U20B2007), the Fundamental Research Funds for the Central Universities (Grant No. 226–2022-00172), and the specialized research projects of Huanjiang Laboratory. The first author of this paper (Shuhua Zeng) gratefully acknowledges the support of the China Scholarship Council (No. 202306320384). We would also like to thank the editors and the reviewers for their constructive comments and helpful suggestions.

AUTHOR DECLARATIONS

Conflict of Interest

The authors have no conflicts to disclose.

Author Contributions

Shuhua Zeng: Investigation (equal); Methodology (equal); Software (equal); Writing – original draft (equal). **Junyua Yang:** Data curation (equal); Investigation (equal). **Wenwen Zhao:** Conceptualization (equal); Funding acquisition (equal); Project administration (equal); Writing – review & editing (equal). **Yifeng Huang:** Investigation (equal). **Zhongzheng Jiang:** Validation (equal). **Weifang Chen:** Funding acquisition (equal).

DATA AVAILABILITY

The data that support the findings of this study are available from the corresponding author upon reasonable request.

REFERENCES

- W. Huang, Z. Du, L. Yan, and Z. Xia, "Supersonic mixing in airbreathing propulsion systems for hypersonic flights," *Prog. Aerosp. Sci.* **109**, 100545 (2019).
- F. Génin and S. Menon, "Dynamics of sonic jet injection into supersonic crossflow," *J. Turbul.* **11**, N4 (2010).
- K. Choi, S. Lee, K. Oh, and C. Kim, "Numerical investigation of jet interactions for a lateral thrust jet controlled interceptor operating at medium altitudes," *Int. J. Aeronaut. Space Sci.* **21**, 39 (2020).
- G. Zhao, C. Zhong, S. Liu, J. Chen, and C. Zhuo, "Numerical simulation of lateral jet interaction with rarefied hypersonic flow over a two-dimensional blunt body," *Phys. Fluids* **35**, 086107 (2023).
- H. Zhuang, D. Ding, H. Chen, G. Li, H. Chen, and B. Zhang, "Effectiveness of reaction control system in hypersonic rarefied reactive flow," *J. Spacecr. Rockets* **59**, 717 (2022).
- J. Huh and S. Lee, "Numerical study on lateral jet interaction in supersonic crossflows," *Aerosp. Sci. Technol.* **80**, 315 (2018).
- B. Srivastava, "Computational analysis and validation for lateral jet controlled missiles," *J. Spacecr. Rockets* **34**, 584 (1997).
- H. Zhen, Z. Gao, and C. Lee, "Numerical investigation on jet interaction with a compression ramp," *Chin. J. Aeronaut.* **26**, 898 (2013).
- K. Mahesh, "The interaction of jets with crossflow," *Annu. Rev. Fluid Mech.* **45**, 379 (2013).
- J. Brandeis and J. Gill, "Experimental investigation of side-jet steering for supersonic and hypersonic missiles," *J. Spacecr. Rockets* **33**, 346 (1996).
- Z. Mahmud and R. D. W. Bowersox, "Aerodynamics of low-blowing-ratio fuselage injection into a supersonic freestream," *J. Spacecr. Rockets* **42**, 30 (2005).
- M. V. Morkovin, C. A. Pierce, and C. E. Craven, "Interaction of a side jet with a supersonic main stream," *Report No. 35* (University of Michigan, Michigan, 1952).
- A. R. Karagozian, "Transverse jets and their control," *Prog. Energy Combust. Sci.* **36**, 531 (2010).
- C. Qiao, H. Xu, J. Li, and H. Hu, "Parametric study on the sonic transverse jet in supersonic crossflow and analysis of the jet-crossflow interaction instability," *Aerosp. Sci. Technol.* **123**, 107472 (2022).
- S. J. Beresh, J. F. Henfling, R. J. Erven, and R. W. Spillers, "Crossplane velocimetry of a transverse supersonic jet in a transonic crossflow," *AIAA J.* **44**, 3051 (2006).
- J. G. Santiago and J. C. Dutton, "Velocity measurements of a jet injected into a supersonic crossflow," *J. Propul. Power* **13**, 264 (1997).
- J. DeSpirito, "Turbulence model effects on cold-gas lateral jet interaction in a supersonic crossflow," *J. Spacecr. Rockets* **52**, 836 (2015).
- S. Yao, W. Zhao, C. Wu, and W. Chen, "Nonlinear constitutive calculation method of rarefied flow based on deep convolution neural networks," *Phys. Fluids* **35**, 096103 (2023).
- S. Mallikarjun, V. Casseau, W. G. Habashi, S. Gao, and A. Karchani, "Hybrid Navier-Stokes-direct simulation Monte Carlo automatic mesh optimization for hypersonics," *J. Thermophys. Heat Transfer* **37**, 779 (2023).
- X. Jin, X. Cheng, Y. Huang, Q. Wang, B. Wang, and Q. Shen, "Numerical analysis of inlet flows at different altitudes in the upper atmosphere," *Phys. Fluids* **35**, 093605 (2023).
- P. L. Bhatnagar, E. P. Gross, and M. Krook, "A model for collision processes in gases—I: Small amplitude processes in charged and neutral one-component systems," *Phys. Rev.* **94**, 511 (1954).
- J. E. Broadwell, "Study of rarefied shear flow by the discrete velocity method," *J. Fluid Mech.* **19**, 401 (1964).
- L. Zhang, W. Ma, Q. Lou, and J. Zhang, "Simulation of rarefied gas flows using physics-informed neural network combined with discrete velocity method," *Phys. Fluids* **35**, 077124 (2023).
- K. Xu and J. Huang, "A unified gas-kinetic scheme for continuum and rarefied flows," *J. Comput. Phys.* **229**, 7747 (2010).
- Z. Guo, K. Xu, and R. Wang, "Discrete unified gas kinetic scheme for all Knudsen number flows: Low-speed isothermal case," *Phys. Rev. E* **88**, 033305 (2013).
- Z. Li and H. Zhang, "Study on gas kinetic unified algorithm for flows from rarefied transition to continuum," *J. Comput. Phys.* **193**, 708 (2004).
- W. Liu, C. Shu, C. Teo, and Z. L. Zhang, "A novel hybrid framework coupling the discrete velocity based-method, the particle-based method and the Grad's distribution function-based method for supersonic rarefied flows," *Aerosp. Sci. Technol.* **131**, 107963 (2022).
- G. Fan, W. Zhao, S. Yao, Z. Jiang, and W. Chen, "The implementation of the three-dimensional unified gas-kinetic wave-particle method on multiple graphics processing units," *Phys. Fluids* **35**, 086108 (2023).
- J. Zhang, B. John, M. Pfeiffer, F. Fei, and D. Wen, "Particle-based hybrid and multiscale methods for nonequilibrium gas flows," *Adv. Aerodyn.* **1**(1), 12 (2019).

- ³⁰J. Zeng, R. Yuan, Y. Zhang, Q. Li, and L. Wu, "General synthetic iterative scheme for polyatomic rarefied gas flows," *Comput. Fluids* **265**, 105998 (2023).
- ³¹S. Liu, C. Zhong, and M. Fang, "Simplified unified wave-particle method with quantified model-competition mechanism for numerical calculation of multi-scale flows," *Phys. Rev. E* **102**, 013304 (2020).
- ³²H. Struchtrup and P. Taheri, "Macroscopic transport models for rarefied gas flows: A brief review," *IMA J. Appl. Math.* **76**, 672 (2011).
- ³³W. Zhao, W. Chen, and R. K. Agarwal, "Formulation of a new set of simplified conventional Burnett equations for computation of rarefied hypersonic flows," *Aerosp. Sci. Technol.* **38**, 64 (2014).
- ³⁴H. Grad, "On the kinetic theory of rarefied gases," *Commun. Pure Appl. Math.* **2**, 331 (1949).
- ³⁵M. Torrilhon, "Modeling nonequilibrium gas flow based on moment equations," *Annu. Rev. Fluid Mech.* **48**, 429 (2016).
- ³⁶M. Fang, Z. Li, Z. Li, J. Liang, and Y. Zhang, "DSMC modeling of rarefied ionization reactions and applications to hypervelocity spacecraft reentry flows," *Adv. Aerodyn.* **2**(1), 7 (2020).
- ³⁷B. C. Eu, *Kinetic Theory and Irreversible Thermodynamics* (Wiley, New York, 1992).
- ³⁸M. Al-Ghoul and B. C. Eu, "Generalized hydrodynamics and shock waves," *Phys. Rev. E* **56**, 2981 (1997).
- ³⁹R. S. Myong, "On the high Mach number shock structure singularity caused by overreach of Maxwellian molecules," *Phys. Fluids* **26**, 056102 (2014).
- ⁴⁰R. S. Myong, "Thermodynamically consistent hydrodynamic computational models for high-Knudsen-number gas flows," *Phys. Fluids* **11**, 2788 (1999).
- ⁴¹J. Yang, X. Li, S. Zeng, W. Zhao, F. Zhang, and W. Chen, "Research on the aero-heating at the sharpened leading edge based on nonlinear coupled constitutive relations," *Chin. J. Theor. Appl. Mech.* **55**, 2321 (2023).
- ⁴²Z. Jiang, W. Zhao, W. Chen, and R. K. Agarwal, "Computation of shock wave structure using a simpler set of generalized hydrodynamic equations based on nonlinear coupled constitutive relations," *Shock Waves* **29**, 1227 (2019).
- ⁴³T. Chourushi, A. Rahimi, S. Singh, O. Ejtehadi, T. K. Mankodi, and R. S. Myong, "Thermal and flow characteristics of nonequilibrium monatomic, diatomic, and polyatomic gases in cylindrical Couette flow based on second-order non-Navier-Fourier constitutive model," *Int. J. Heat Mass Transfer* **187**, 122580 (2022).
- ⁴⁴R. S. Myong, "A full analytical solution for the force-driven compressible Poiseuille gas flow based on a nonlinear coupled constitutive relation," *Phys. Fluids* **23**, 012002 (2011).
- ⁴⁵Z. Jiang, W. Zhao, Z. Yuan, W. Chen, and R. S. Myong, "Computation of hypersonic flows over flying configurations using a nonlinear constitutive model," *AIAA J.* **57**, 5252 (2019).
- ⁴⁶S. Zeng, Y. Qiu, Z. Jiang, and W. Chen, "Experimental validation of nonlinear coupled constitutive relations in continuum flows," in *Proceedings of the 2021 Asia-Pacific International Symposium on Aerospace Technology (APISAT 2021)*, edited by S. Lee, C. Han, J. Choi, S. Kim, and J. H. Kim (Springer, Singapore, 2023), Vol. 1, p. 292.
- ⁴⁷S. Zeng, W. Zhao, Z. Jiang, and W. Chen, "Numerical investigation and experimental validation of nonlinear constitutive models with solving algorithms in continuum flows," *J. Aerosp. Power* **39**, 1-12 (2023).
- ⁴⁸Z. Yuan, W. Zhao, Z. Jiang, W. Chen, and R. K. Agarwal, "Modified nonlinear coupled constitutive relations model for hypersonic nonequilibrium flows," *J. Thermophys. Heat Transfer* **34**, 848 (2020).
- ⁴⁹O. Ejtehadi, T. K. Mankodi, I. Sohn, B. J. Kim, and R. S. Myong, "Gas-particle flows in a microscale shock tube and collection efficiency in the jet impingement on a permeable surface," *Phys. Fluids* **35**, 103324 (2023).
- ⁵⁰S. Singh, A. Karchani, T. Chourushi, and R. S. Myong, "A three-dimensional modal discontinuous Galerkin method for the second-order Boltzmann-Curtiss-based constitutive model of rarefied and microscale gas flows," *J. Comput. Phys.* **457**, 111052 (2022).
- ⁵¹S. Zeng, Z. He, W. Zhao, and W. Chen, "A computational strategy for nonlinear coupled constitutive relations of rarefied nonequilibrium flows on unstructured grids," *Aerosp. Sci. Technol.* **141**, 108477 (2023).
- ⁵²Z. He, Z. Jiang, H. Zhang, and W. Chen, "Analytical method of nonlinear coupled constitutive relations for rarefied non-equilibrium flows," *Chin. J. Aeronaut.* **34**, 136 (2021).
- ⁵³Z. Jiang, W. Zhao, W. Chen, and R. K. Agarwal, "An undecomposed hybrid algorithm for nonlinear coupled constitutive relations of rarefied gas dynamics," *Commun. Comput. Phys.* **26**, 880 (2019).
- ⁵⁴Z. Jiang, W. Chen, and W. Zhao, "Numerical analysis of the micro-Couette flow using a non-Newton-Fourier model with enhanced wall boundary conditions," *Microfluid. Nanofluid.* **22**(1), 10 (2018).
- ⁵⁵S. Zeng, W. Zhao, Z. Jiang, and W. Chen, "A second-order slip/jump boundary condition modified by nonlinear Rayleigh-Onsager dissipation factor," *Phys. Fluids* **35**, 042001 (2023).
- ⁵⁶Z. Yuan, Z. Jiang, W. Zhao, and W. Chen, "Multiple temperature model of nonlinear coupled constitutive relations for hypersonic diatomic gas flows," *AIP Adv.* **10**, 055023 (2020).
- ⁵⁷T. K. Mankodi and R. S. Myong, "Boltzmann-based second-order constitutive models of diatomic and polyatomic gases including the vibrational mode," *Phys. Fluids* **32**, 126109 (2020).
- ⁵⁸Z. Yuan, W. Zhao, Z. Jiang, and W. Chen, "Numerical simulation of hypersonic reaction flows with nonlinear coupled constitutive relations," *Aerosp. Sci. Technol.* **112**, 106591 (2021).
- ⁵⁹S. Zeng, Z. Yuan, W. Zhao, and W. Chen, "Numerical simulation of hypersonic thermochemical nonequilibrium flows using nonlinear coupled constitutive relations," *Chin. J. Aeronaut.* **36**, 63 (2023).
- ⁶⁰Y. Huang, S. Zeng, Z. Jiang, and W. Chen, "Numerical study on high-altitude lateral jet based on nonlinear coupled constitutive relation," *Acta Aeronaut. Astronaut. Sin.* **43**, 727700 (2022).
- ⁶¹Y. Huang, Z. Jiang, S. Zeng, and W. Chen, "Numerical study of high altitude reverse jet based on nonlinear coupled constitutive chemical-reaction model," *J. Aerosp. Power* (published online 2023).
- ⁶²M. Al-Ghoul and B. C. Eu, "Generalized hydrodynamic theory of shock waves: Mach-number dependence of inverse shock width for nitrogen gas," *Phys. Rev. Lett.* **86**, 4294 (2001).
- ⁶³S. Liu, Y. Yang, and C. Zhong, "An extended gas-kinetic scheme for shock structure calculations," *J. Comput. Phys.* **390**, 1-24 (2019).
- ⁶⁴E. V. Kustova, E. A. Nagnibeda, Y. D. Shevelev, and N. G. Syzranova, "Comparison of different models for non-equilibrium CO₂ flows in a shock layer near a blunt body," *Shock Waves* **21**, 273 (2011).
- ⁶⁵R. N. Gupta, J. M. Yos, and R. A. Thompson, "A review of reaction rates and thermodynamic and transport properties for the 11-species sir model for chemical and thermal nonequilibrium calculations to 30000 K," Technical Memorandum No. NASA RP-1232 (NASA Langley Research Center, Hampton, Virginia, 1989).
- ⁶⁶P. A. Gnoffo, R. N. Gupta, and J. L. Shinn, "Conservation equations and physical models for hypersonic air flows in thermal and chemical nonequilibrium," Report No. NASA-TP-2867 (NASA Langley Research Center, Hampton, VA, 1989), available at <https://ntrs.nasa.gov/citations/19890006744>.
- ⁶⁷C. Park, "Assessment of a two-temperature kinetic model for dissociating and weakly ionizing nitrogen," *J. Thermophys. Heat Transfer* **2**, 8 (1988).
- ⁶⁸G. S. R. Sarma, "Physico-chemical modelling in hypersonic flow simulation," *Prog. Aerosp. Sci.* **36**, 281 (2000).
- ⁶⁹J. D. Anderson, *Hypersonic and High Temperature Gas Dynamics*, 2nd ed. (American Institute of Aeronautics and Astronautics, Inc., Virginia, 2006).
- ⁷⁰R. C. Millikan and D. R. White, "Systematics of vibrational relaxation," *J. Chem. Phys.* **39**, 3209 (1963).
- ⁷¹C. R. Wilke, "A viscosity equation for gas mixtures," *J. Chem. Phys.* **18**, 517 (1950).
- ⁷²R. N. Gupta, K. Lee, R. A. Thompson, and J. M. Yos, "Calculations and curve fits of thermodynamic and transport properties for equilibrium air to 30000 K," Report No. NASA-RP-1260 (NASA Langley Research Center, Hampton, VA, 1991).
- ⁷³R. Maccormack, "The computation of hypersonic ionized flows in chemical and thermal nonequilibrium," AIAA Paper No. 88-0511, 1988.
- ⁷⁴R. S. Myong, "A generalized hydrodynamic computational model for rarefied and microscale diatomic gas flows," *J. Comput. Phys.* **195**, 655 (2004).
- ⁷⁵X. Wang, C. Yan, W. Zheng, K. Zhong, and Y. Geng, "Laminar and turbulent heating predictions for mars entry vehicles," *Acta Astronaut.* **128**, 217 (2016).
- ⁷⁶X. Chai, P. S. Iyer, and K. Mahesh, "Numerical study of high speed jets in cross-flow," *J. Fluid Mech.* **785**, 152 (2015).
- ⁷⁷P. Champigny and R. G. Lacau, "Lateral jet control for tactical missiles," AGARD Report No. 804 (1994), pp. 1-57.
- ⁷⁸V. Viti, R. Neel, and J. A. Schetz, "Detailed flow physics of the supersonic jet interaction flow field," *Phys. Fluids* **21**, 046101 (2009).

- ⁷⁹Y. Liu, M. Sun, Y. Yang, C. Liang, J. Yu, and H. Wang, "Turbulent boundary layer subjected to a sonic transverse jet in a supersonic flow," *Aerosp. Sci. Technol.* **104**, 106016 (2020).
- ⁸⁰J. Zhang, Y. Cui, J. Cai, and H. Dou, "Numerical Investigation of Lateral Jets Over Body of Revolution in Supersonic Crossflow," *J. Propul. Power* **28**, 33 (2012).
- ⁸¹R. Roger, "The aerodynamics of jet thruster control for supersonic/hypersonic endo-interceptors: Lessons learned," AIAA Paper No. 99-0804, 1999.
- ⁸²R. H. Nunn, "Jet interaction wrap-around on bodies of revolution," *J. Spacecr. Rockets* **7**, 334 (1970).
- ⁸³B. Y. Min, J. W. Lee, and Y. H. Byun, "Numerical investigation of the shock interaction effect on the lateral jet controlled missile," *Aerosp. Sci. Technol.* **10**, 385 (2006).